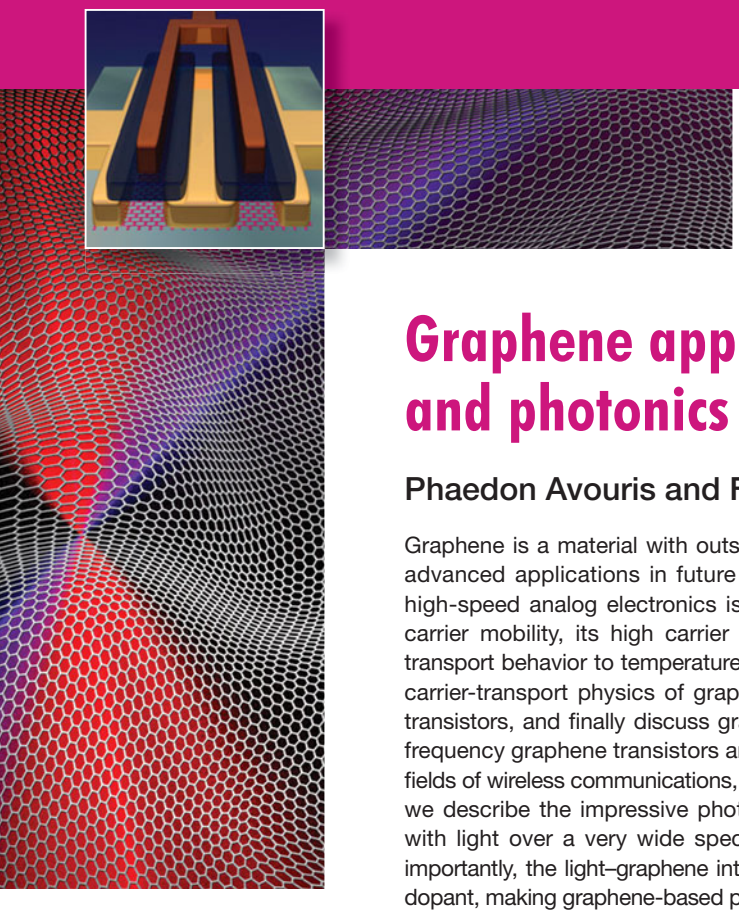

Graphene applications in electronics and photonics

Phaedon Avouris and Fengnian Xia

Graphene is a material with outstanding properties that make it an excellent candidate for advanced applications in future electronics and photonics. The potential of graphene in high-speed analog electronics is currently being explored extensively because of its high carrier mobility, its high carrier saturation velocity, and the insensitivity of its electrical-transport behavior to temperature variations. Herein, we review some of the key material and carrier-transport physics of graphene, then focus on high-frequency graphene field-effect transistors, and finally discuss graphene monolithically integrated circuits (ICs). These high-frequency graphene transistors and ICs could become essential elements in the blossoming fields of wireless communications, sensing, and imaging. After discussing graphene electronics, we describe the impressive photonic properties of graphene. Graphene interacts strongly with light over a very wide spectral range from microwaves to ultraviolet radiation. Most importantly, the light–graphene interaction can be adjusted using an electric field or chemical dopant, making graphene-based photonic devices tunable. Single-particle interband transitions lead to a universal optical absorption of about 2% per layer, whereas intraband free-carrier transitions dominate in the microwave and terahertz wavelength range. The tunable plasmonic absorption of patterned graphene adds yet another dimension to graphene photonics. We show that these unique photonic properties of graphene over a broad wavelength range make it promising for many photonic applications such as fast photodetectors, optical modulators, far-infrared filters, polarizers, and electromagnetic wave shields. These graphene photonic devices could find various applications in optical communications, infrared imaging, and national security.

Carrier transport in graphene

Graphene has some outstanding physical properties that make it extremely appealing for applications in electronics. Of these, the extraordinarily rapid charge-carrier transport of graphene has received the most attention, and mobilities[1,2] in excess of 200,000 $cm^2\ V^{-1}\ s^{-1}$ and saturation velocities[3] of $\sim 5 \times 10^7$ cm s^{-1} have been reported. In addition, the one-atom thickness, mechanical strength, flexibility, high current-carrying capacity (up to 10^9 A/cm^2), and high thermal conductivity (up to 50 W $cm^{-1}\ K^{-1}$)[4] of graphene all contribute to its appeal.

Most of these record properties refer to a pristine material under somewhat idealized conditions. In technology, however, graphene is part of a more complex structure and is used under conditions that are dictated by the application. Under such realistic conditions, electronic transport is subject to a variety of scattering interactions,[5–10] including long-range interactions with charged impurities on graphene or the supporting insulator substrate and short-range interactions involving neutral defects or adsorbates, surface roughness, and phonons.

Which of these mechanisms dominates the scattering depends on both the quality of the graphene sample and the characteristics of its environment.[11] For instance, Coulomb scattering from charged impurities typically dominates at low temperatures for graphene on insulating substrates (e.g., SiO_2, SiC, Al_2O_3).[7] Even in suspended graphene, transport is influenced by adsorbed species, so the mobility is greatly enhanced after these species are volatilized by heating.[1,2] When all impurities and structural defects are eliminated, phonon scattering remains.

The magnitude of the carrier mobility (μ) and its dependence on temperature (T) and carrier density (n) are indicative of the dominant scattering mechanism.[11] Thus, mobilities that are greater than about 100,000 $cm^2\ V^{-1}\ s^{-1}$ and are proportional to $1/nT$ indicate transport dominated by acoustic-phonon scattering, whereas Coulomb scattering typically leads to mobilities on the

Phaedon Avouris, IBM, Watson Research Center; avouris@us.ibm.com
Fengnian Xia, IBM, Watson Research Center; fxia@us.ibm.com
DOI: 10.1557/mrs.2012.206

order of 1000–10,000 $cm^2 V^{-1} s^{-1}$ that are independent of n, and short-range scattering by neutral defects leads to a temperature-independent mobility that is proportional to $1/n$.[5,9,12–14]

Although a number of different electronic devices based on graphene can be envisioned, we focus here on the most widely explored concept, that of field-effect transistors. Transport in graphene is intrinsically ambipolar, meaning that both positive and negative carriers are important. As illustrated in **Figure 1**a–b, when, through application of the appropriate gate bias, the Fermi level, E_F, is brought below the neutrality point, E_{NP} (the energy of the Dirac point), transport involves holes, whereas for $E_F > E_{NP}$, electrons are transported. As the Fermi energy is changed by the gate, the density of states (DOS) and, correspondingly, the carrier density ($n \propto E_F^2$) are changed. This is the basis of "switching" in graphene field-effect transistors (GFETs).

However, unlike transistors made of conventional semiconductors with a bandgap, a GFET does not turn off completely, even though the DOS is zero at the neutrality point. A residual conductivity, the so-called minimum conductivity (σ_{min}), remains.[16] This is illustrated in Figure 1c, which shows the variation of the minimum conductivity as a function of the width-to-length ratio (W/L) for a graphene FET.[15,17] As can be seen, the conductivity decreases with increasing W/L, and at a high ratio, it approaches the theoretically predicted value[15] of $4e^2/\pi h$.

The fact that the current in the graphene channel cannot be completely shut off by the gate limits the achievable current on/off ratio to around 10, although the exact value depends on the quality of the graphene and the effectiveness of the gating. Figure 1d shows the variation of the on/off ratio as a function of the channel length of a GFET operated in the p and n branches of graphene at 4.3 K.[15] The origin of the variation is discussed later in this section. The key point is that digital transistors used in logic applications require on/off ratios higher than about 10^4. It is therefore clear that graphene in its natural form is not appropriate for a digital switch.

The operation of graphene devices is not only dependent on the electrical properties of the graphene material used, but is also strongly affected or even dominated by what happens in other parts of the device. Specifically, carriers have to be injected into a graphene channel and then collected through metal contacts. These contacts generate potential energy barriers for carriers, similar to the Schottky barriers in conventional semiconductors that strongly affect the performance of those devices. Graphene and metals typically have different work functions, which causes charge transfer between them. This charge transfer leads to the doping of graphene underneath the metal and induces a local band bending. If more-reactive metals such as nickel or platinum are used, there can be significant hybridization and modification of the graphene band structure under them.

A carrier injected into graphene from the metal must overcome or tunnel through a barrier formed at the metal–graphene interface by the charge-transfer process and also another barrier generated at the junction between the thus-doped graphene under the metal and the graphene of the channel (a doping barrier similar to a p–n junction).[18–20] Typically, tunneling through this barrier is described as a form of Klein tunneling (gapless interband tunneling).[21,22] This transmission ultimately depends on the steepness of the barrier near E_F and the angle of incidence.

In practice, experimental factors such as improper metal adhesion and the presence of metal oxides, other impurities, and roughness at the metal–graphene interface can make important contributions to the measured contact resistance. For these reasons, the experimental values of metal–graphene contact resistance tend to vary significantly, from a couple

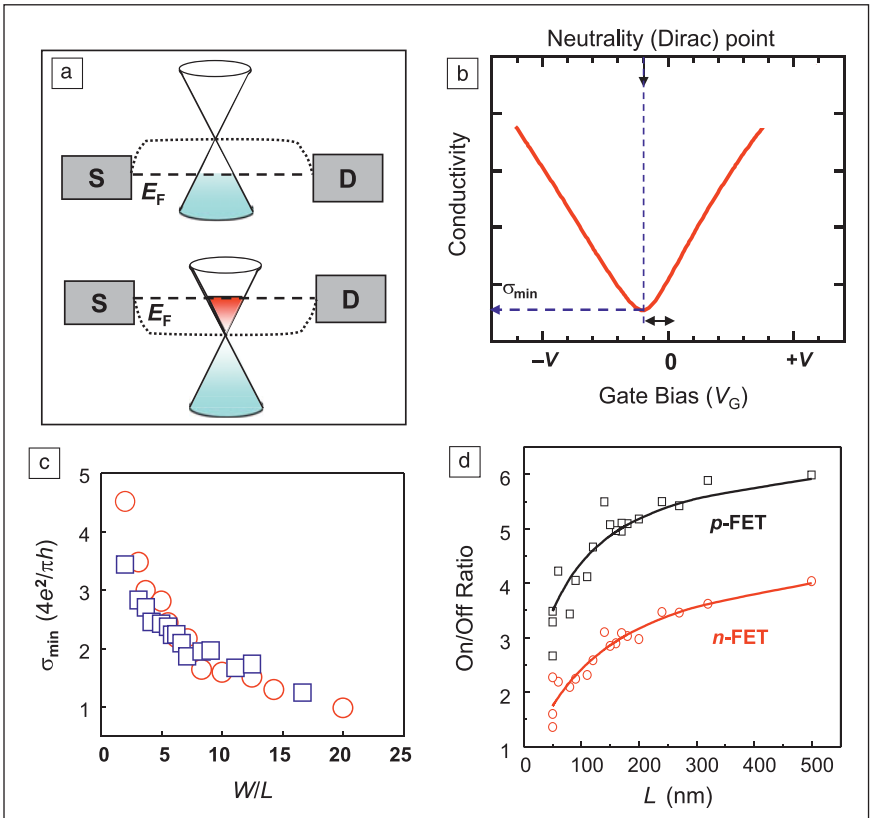

Figure 1. General electrical characteristics of a graphene field-effect transistor (GFET): (a) Ambipolar operation: (Top) Hole conduction between source S and drain D occurs when the Fermi energy E_F lies below the neutrality (Dirac) point where the bands meet. (Bottom) Electron conduction occurs when E_F lies above the neutrality point. (b) Schematic of GFET conductivity versus gate voltage (V_G), illustrating the minimum conductivity, σ_{min}. (c) Variation of σ_{min} (scaled to the theoretical minimum conductance $4e^2/\pi h$, where e is the electron charge and h is Planck's constant) of a GFET as a function of the channel width-to-length ratio (W/L) at 300 K (red) and 4.3 K (blue). (d) Ratio of the on current (with a large gate voltage) to the off current (at the minimum) of a GFET as a function of the channel length L. Reproduced with permission from Reference 15. ©2012, American Chemical Society.

hundred to several thousand ohm micrometers.[20] Moreover, the value of the contact resistance is a function of the gate voltage, because of the varying density of states, and is also weakly dependent on temperature.[20]

Critically, the contact resistances are comparable to the resistance of the graphene channel itself. Furthermore, the high contact resistance becomes more significant as the channel length is scaled down and more of the potential drop occurs at the contacts. Eventually, when transport in the channel becomes ballistic, contacts dominate the function of devices.[15] This behavior is demonstrated in **Figure 2**, which shows the resistance of back-gated devices with different channel lengths as a function of the difference of the back-gate voltage from the Dirac point. The work function of palladium used as the contact metal in this case is high, so charge transfer leads to hole (p) doping of the graphene under the metal.

In the device with the longest channel shown (250 nm), the doping profile along the channel varies depending on the bias of the gate (V_G) with respect to the Dirac voltage (V_{Dirac}, the gate voltage for which the maximum longitudinal resistivity occurs): It is p'–p–p' (where p and p' indicate two different degrees of hole doping) for $V_G - V_{Dirac} < 0$, but becomes p–n–p for $V_G - V_{Dirac} > 0$. The formation of p–n junctions leads to a larger resistance for electrons than for holes, breaking the electron–hole transport symmetry of graphene.[21,22] As the channel length is decreased, the asymmetry becomes more pronounced. Finally, in the shortest device studied (50 nm), transport is quasiballistic (almost free of scattering) and coherent: Not only is the asymmetry very pronounced, but the electron transport shows a clear oscillatory behavior.[15] Experiment and theoretical modeling have shown that these oscillations are due to electron reflection and quantum interference produced by the potential barriers introduced by the contacts, that is, the channel acts as a Fabry–Perot cavity.[15]

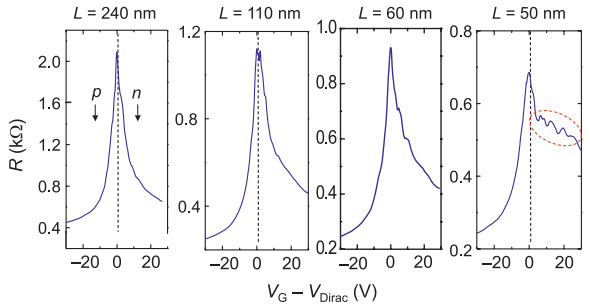

Figure 2. Resistance (R) of a back-gated GFET prepared by chemical vapor deposition (CVD) as a function of the difference between the gate voltage (V_G) and the Dirac voltage (V_{Dirac}) in devices with different channel lengths (L), demonstrating the role of metal contacts in electron- and hole-transport asymmetry. The contact metal is palladium, which dopes graphene p-type. As the channel length decreases, the resistance for electron transport ($V_G > V_{Dirac}$) increases, reflecting the formation of a p–n–p structure and the increasing relative contribution of the contacts to the overall resistance. For the shortest channel (L = 50 nm), transport is quasiballistic and coherent, and the carriers reflected by the contact barriers show quantum interference and Fabry–Perot-like oscillations (indicated by the red dashed oval). Reproduced with permission from Reference 15. ©2012, American Chemical Society.

Graphene transistors and circuits

Whereas the lack of a bandgap and the resulting incomplete switching of graphene do not support its use as a digital switch, the outstanding carrier mobility of graphene, the high transconductance of graphene devices, and the ultimate thinness and stability of the material make it an excellent choice for fast analog electronics, specifically radio-frequency (RF) transistors. In analog RF operation, the ability to completely switch off the device, although desirable, is not necessary. For example, in signal amplifiers, a major application of this type of device, the transistor is always in the on state, and the RF signal to be amplified is superimposed on the dc gate bias.

Whereas the easy preparation of graphene by graphite exfoliation[23] provided the impetus for the development of the graphene field, this method is not appropriate for large-scale industrial production. In particular, in electronics technology, one needs large-scale graphene on an insulating substrate. Furthermore, to be able to use the already highly advanced silicon device processing techniques in graphene technology, graphene in wafer form is highly desirable.

Currently, two general types of methods for the large-scale synthesis of graphene are utilized, as discussed in the articles by Nyakiti et al. and Bartelt and McCarty in this issue of *MRS Bulletin*. One is based on the thermal decomposition of SiC.[24–28] When SiC wafers are heated, typically in the presence of an argon atmosphere, at temperatures on the order of 1500°C, silicon desorbs, and the remaining carbon rebonds to form (depending on the experimental conditions) one or more layers of graphene on top of the SiC, which itself acts as the insulating substrate. Both the growth rate and the characteristics of the resulting graphene depend on whether the silicon-terminated or carbon-terminated face of SiC is used for growth. Growth is much faster on the carbon face, leading to multilayer graphene with many surface wrinkles and a material that tends to be p-doped after exposure to the environment. Silicon-face growth is slower, can be controlled, and typically gives rise to n-type graphene.

Another widely used approach involves the growth of graphene on metals. Two main mechanisms for growth have generally been employed. One involves catalytic metals such as nickel, ruthenium, platinum, and iron, which not only can dissociate the carbon precursors (e.g., CH_4, C_2H_2) but can also dissolve significant amounts of carbon at high temperature.[29,30] Upon cooling, the carbon segregates as graphene on the metal surface. The other approach is a catalytic chemical vapor deposition (CVD) process whereby the precursor is decomposed at elevated temperatures (>1000°C) on copper, which has very limited solubility for carbon.[31,32] This simple, rather inexpensive technique yields primarily monolayer graphene and has the advantage that, after the dissolution of the copper, the thus-formed monolayer can be transferred

to another substrate, such as any of the optically transparent substrates used in photonic applications. Once a graphene film is in place, devices can be fabricated in it using electron-beam or photolithography, and oxygen plasma can be used to etch away the unwanted graphene. Metal contacts are formed using some form of metal evaporation.

A key materials issue encountered in the fabrication of graphene devices involves finding an appropriate gate dielectric insulator and substrate. To optimize the field effect of the gate, a very thin high-dielectric-constant film is needed. Graphene is both inert and hydrophobic. Therefore, very thin polar insulators (e.g., SiO_2, HfO_2, Al_2O_3) form poor-quality, nonuniform, and leaky films on it. In addition, such materials tend to trap charges near or at the insulator–graphene interface, leading to Coulomb scattering and a dramatic decrease in carrier mobility.[33] A number of different approaches have been used to address this problem, including deposition of a thin, inert buffer layer that wets the surface before atomic-layer deposition (ALD) of the main film,[33] plasma-assisted deposition of Si_3N_4,[34] or deposition of a thin metal film seed layer (usually aluminum) that is then oxidized in situ prior to ALD of the insulator film.[35]

Because graphene produced by different methods is unintentionally *p*- or *n*-doped, there is a need to shift the neutrality point close to $V_G = 0$ V. This can be accomplished through compensation by choosing the appropriate insulator, for example, AlO_x for CVD graphene or SiN_x for epitaxial graphene. A schematic of the structure and a colorized image of a fabricated RF GFET are shown in **Figure 3**a–b.[36] See the sidebar for a description of some metrics used to evaluate GFETs.

The first experimental graphene transistors used graphene exfoliated from graphite and deposited on SiO_2 to initially make dc[38,39] and later RF[36,37,40–46] GFET devices. The first technologically relevant efforts utilizing wafer-scale synthesized graphene were based on the thermal decomposition of SiC.[40–44] A highly encouraging result came in 2010, when wafer-scale RF GFETs were produced with f_T values of 100 GHz.[44] However, the lack of a bandgap, the high optical-phonon frequency in graphene, and the presence of defects made current saturation hard to achieve; g_d was large, and thus voltage gain was low.

In these early studies, however, the graphene used had a rather modest mobility of ~1500 $cm^2 V^{-1} s^{-1}$, and the gate length was, by today's silicon-industry standards, quite long (240 nm), suggesting that dramatic enhancements in performance could be achieved by additional materials and device improvements. Indeed, the second generation of SiC-based GFETs attained f_T values exceeding 300 GHz, in part by employing channel lengths as low as 40 nm[17] (see Figure 3c), and voltage gains up

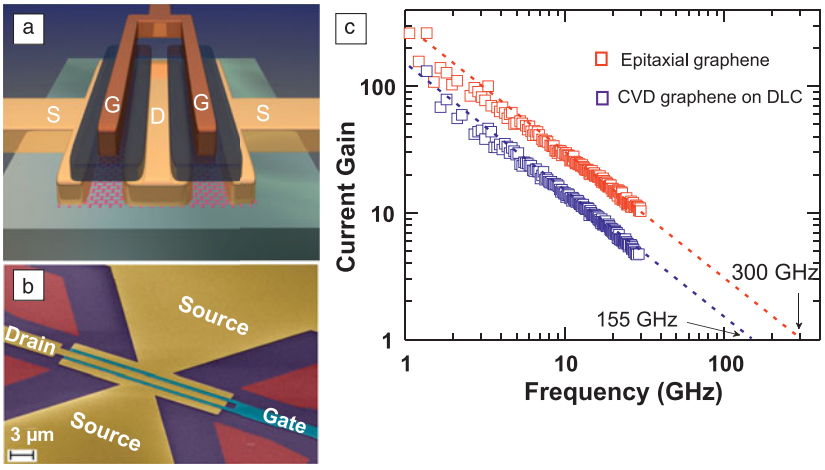

Figure 3. (a) Schematic and (b) colorized optical image of a top-gated GFET, in which the voltage on the gate (G) controls the current flowing in the underlying graphene between the source (S) and drain (D). In both cases, the tan region including the source and drain represents graphene. (c) Current gains of two radio-frequency (RF) GFETs as functions of frequency. One (blue squares) is a CVD graphene FET on a diamond-like carbon (DLC) film for which the current gain extrapolates to unity at f_T = 155 GHz,[37] and the other (red squares) is an epitaxial graphene FET from SiC with f_T = 300 GHz.[36]

GFET Metrics

Several metrics are used to evaluate GFETs. Assessment of the intrinsic capabilities of a new channel material, such as graphene, should be insensitive to contact resistance and fabrication details. The metric used for this purpose is the cutoff frequency, f_T, which is defined as the frequency at which the current gain becomes 1 when the drain is short-circuited to the source. In a well-behaved device, f_T is given by $f_T = g_m/2\pi C$, where g_m ($g_m = dI/dV_G$) and C are the transconductance and gate capacitance of the device, respectively.[3]

In contrast to this indicator of ultimate potential, for working devices, it is the voltage gain that is usually demanded. This voltage gain is defined as the ratio of the output voltage (at the drain) to the input voltage (at the gate) and is given by the ratio of the transconductance, g_m, to the output conductance, g_d ($g_d = dI/dV_d$). High voltage gain requires g_m to be as high as possible and g_d to be as small as possible. The latter condition requires that the transistor be operated at conditions of current saturation, where the current is almost independent of V_d.

Many applications also require power gain, for which the appropriate metric is the maximum frequency, f_{max}, which is the frequency at which the unilateral power gain becomes unity.[3] This metric is strongly dependent not only on the channel material (i.e., graphene), but also on the actual structure of the device.

to 20 dB were obtained with optimized device architectures. Operation closer to current-saturation conditions and use of thinner gate oxides have already produced an improved f_{max} value of ~40 GHz.[17,36]

The development of CVD graphene that can be transferred onto any substrate also provided the opportunity for a wide selection of substrates. The commonly used SiO_2 is hydrophilic and prone to containing charged defects, both of which substantially degrade the value and reproducibility of the mobility in GFETs. One alternative substrate that was used successfully is diamond-like carbon (DLC), which is fully compatible with graphene, readily available, hydrophobic, and nonpolar. Initial results with this substrate yielded GFETs with f_T = 155 GHz (see Figure 3c),[37] and recent improvements have led to f_T = 300 GHz.[17,36] Most significantly, a study of the temperature dependence of GFETs on DLC showed that the performance remains essentially the same from 300 K to 4 K, indicating the absence of carrier freeze-out and demonstrating that graphene electronics could be used in extreme environments, such as outer space.[37]

Thin layers of exfoliated, single-crystal, hexagonal boron nitride (h-BN) have also been used successfully as both the gate insulator and the substrate for graphene transistors.[47,48] h-BN is an isomorph of graphite with a large bandgap (~6 eV), making it an ideal insulator in this case. Single layers of graphene on h-BN were found to exhibit enhanced carrier mobilities (>100,000 $cm^2\ V^{-1}\ s^{-1}$) and reduced carrier inhomogeneity and doping compared with graphene on SiO_2, leading to scattering mean free paths on the order of 1 μm.[47–49] Boron nitride appears to be an ideal material for building graphene devices, provided that fabrication processes such as high-quality CVD can be developed that preserve the qualities of h-BN that is exfoliated from crystals.[50,51]

The intrinsic cutoff frequency of graphene transistors has already reached the range of 100–400 GHz, demonstrating that, with further development, graphene technology can be competitive with other well-established RF technologies such as GaAs or InP high-electron-mobility transistors (f_T = 100–600 GHz). A performance gap still exists, however, between graphene and the other mature technologies with respect to gain, f_{max}.[3] We note that, rather than representing the intrinsic performance of graphene, f_{max} is a metric that is strongly affected by the extrinsic components and layout of the circuit, and therefore, this performance gap can be reduced through further improvement of these other aspects.

In addition to efforts to enhance the performance of individual GFETs, initial results on device integration into circuits are appearing. A number of problems have to be resolved, primarily adapting technologies developed for silicon technology to the special requirements of graphene, such as adhesion to metals and electrical isolation. The contacts also limit how densely graphene devices can be packed. The transfer length required to achieve the lowest contact resistance, typically on the order of 100 nm for graphene,[20] could eventually determine the ultimate pitch of the devices.

The first monolithically integrated graphene circuit, reported in 2011, involved a gigahertz-frequency unipolar mixer based on epitaxially grown graphene[46] (see **Figure 4**). This one-transistor integrated circuit (IC) mixed two microwave signals to generate sum-frequency and difference-frequency signals and demonstrated the advantage that graphene offers in such applications because of the insensitivity of the resulting mixer performance to temperature variations. Earlier, frequency mixing based on the ambipolar behavior of graphene was successfully demonstrated.[52] A key application of analog transistors involves RF signal amplification. Other published demonstrations include an audio-range

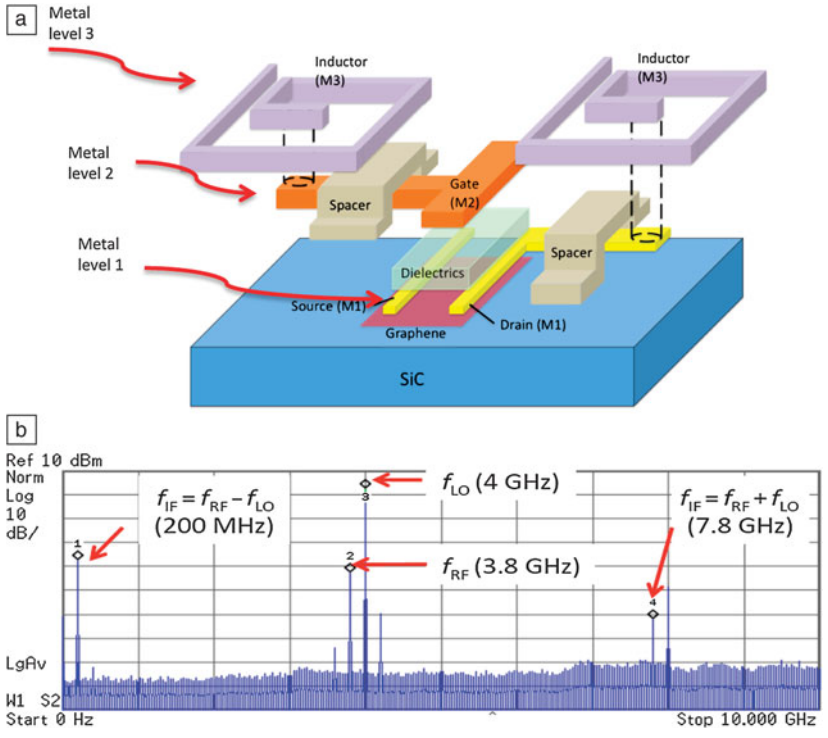

Figure 4. Graphene frequency-mixer integrated circuit (IC). (a) Schematic illustration of a graphene mixer. The key components include a top-gated graphene transistor and two inductors connected to the gate and the drain of the GFET. Three distinct metal layers of the graphene IC are represented by M1, M2, and M3. A layer of 120-nm-thick SiO_2 is used as the isolation spacer to electrically separate the inductors (M3) from the underlying interconnects (M1 and M2). (b) Output spectrum of the mixer between 0 GHz and 10 GHz using an input RF frequency of f_{RF} = 3.8 GHz and a local-oscillator frequency of f_{LO} = 4 GHz. Each *x* and *y* division corresponds to 1 GHz and 10 dB, respectively. The frequency mixing is observed as two peaks (f_{IF}) at the difference and sum frequencies 200 MHz and 7.8 GHz, respectively. Reproduced with permission from Reference 46. ©2011, American Association for the Advancement of Science.

(kilohertz) amplifier using exfoliated graphene[53] and wafer-scale IC structures.[17,54]

Graphene photonics

Graphene interacts very strongly with light. In the near-infrared and visible regions of the electromagnetic spectrum, where the electronic dispersion relation of graphene is nearly linear, suspended graphene in air absorbs about 2.3% of the normally incident light (calculated as $\pi\alpha$, where $\alpha = e^2/\hbar c \approx 1/137$ is the fine structure constant).[55,56] This implies an absorption coefficient for single-layer graphene (of thickness $t_G = 3.35$ Å) of $-\ln(1 - \pi\alpha)/t_G \approx 7 \times 10^5$ cm^{-1}, which is one to three orders of magnitude higher than those of technologically relevant photonic materials such as $In_{0.53}Ga_{0.47}As$, GaAs, and germanium at 1.55 μm.[55] A number of experimental studies have verified the ~2.3% absorption per layer at visible and near-infrared energies.[55,57,58] Moreover, the absorption of graphene multilayers is approximately additive, if one excludes the energy region below 0.5 eV, where the absorption depends on both the number of layers and their stacking.

Studies of graphene absorption over broad energy ranges[59,60] have become available more recently. As seen in **Figure 5**a, at energies above the infrared region, the absorption increases steadily, peaks at about 4.6 eV, and has an asymmetric line shape.[59] This is the range expected for π–π* interband transitions at the saddle-point singularity near the high-symmetry *M* point of the graphene Brillouin zone (see Figure 5b). However, *ab initio* calculations, using the well-known GW approximation (G stands for Green's function, and *W* is the screened Coulomb interaction), predict the energy of this transition to be significantly higher, 5.2 eV.[61] These observations can be explained by the presence of strong electron–hole interactions that form a saddle-point exciton and red shift the excitation energy. The asymmetric line shape develops through Fano-type interference between this exciton and the continuum of interband transitions near the *M* point.[59,60,62]

Interband excitations of graphene decay very rapidly. Pulsed excitation generates electron–hole pairs in a nonequilibrium state. Electron–electron interactions lead to a fast redistribution of energy, which, in turn, leads to a Fermi–Dirac distribution with a high electron temperature, T_e.[62,63] This process takes place in 100–300 fs and depends on the carrier concentration/doping. The lattice is heated on a picosecond time scale by optical-phonon emission.[62,63] When the remaining energy falls below the optical-phonon energy (~200 meV), acoustic-phonon emission, which proceeds slowly (on the order of nanoseconds),[64] provides an energy-dissipation bottleneck. The fast decay of graphene excitations leads to the absence of resonant fluorescence, allows the fast recovery of saturated absorption exploited in Q switching, and affects the size of photocurrents, whereas the "hot" carriers resulting from the acoustic-phonon bottleneck play a role in the generation of photothermoelectric effects.

In the presence of a field gradient, photoexcitation of graphene can produce a photocurrent, which can be used in a number of optoelectronic applications. As a photodetector, graphene has the advantages of having a very wide absorption range, having a fast time response due to the high mobilities of both electrons and holes, being a thin and low-cost material, and having the ability to operate at ambient temperature. The required electric field could be simply produced by applying a voltage bias. However, because graphene does not have a bandgap, this would produce a sizable dark current, leading to heating and excessive shot and thermal noise.

For these reasons, the use of internal fields is desirable for photodetection. Such fields are present at metal–semiconductor junctions (Schottky junctions). These junctions form naturally at metal–graphene contacts as a result of work-function differences between the two materials,[20] or they can be formed by, for example, differential doping of graphene[65] or fabrication of split-gate devices.[66] The carriers are driven by the potential gradient at the *p–n* junction[67–70] and by photothermal effects (PTEs),[71–73] which can arise because of laser-induced heating and the difference in Seebeck coefficients, *S*, of the two differently doped sides, $V_{PTE} = (S_2 - S_1)\Delta T$. Even in the case of photothermal effects, the response can be fast because the hot carriers ($T_e > T_{lattice}$) produced by the acoustic-phonon bottleneck, which transport the heat, have a much lower heat capacity than phonons.[72]

So far, we have focused on the spectral properties of graphene arising from interband transitions. In the far-infrared and terahertz regions,

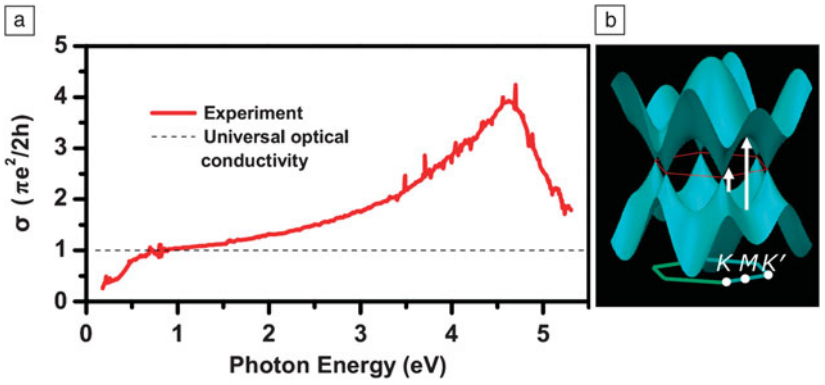

Figure 5. Absorption spectrum of graphene. (a) Optical conductivity (solid line) and "universal" optical conductivity $\pi e^2/2h$ (dashed line) of monolayer graphene in the spectral range of 0.2–5.5 eV. The experimental peak energy is 4.6 eV. The deviation of the optical conductivity from the universal value at energies below 1 eV is attributed to Pauli blocking of the absorption due to the doping of the sample. Part (a) reproduced with permission from Reference 59. ©2011, American Physical Society. (b) Schematic of the band structure of graphene. Interband transitions near the *K* point (short vertical arrow) give rise to the universal absorption. The saddle point at the *M* point and the associated excitons (long vertical arrow) give rise to the conductivity peak, and interference with the interband absorption causes its asymmetry.

however, intraband transitions or free-carrier absorption dominates. The frequency dependence of the free-carrier response in graphene can be adequately described by the Drude model of metallic absorption, in which the dynamical conductivity at angular frequency ω is given by $\sigma(\omega) = iD/[\pi(\omega + i\Gamma)]$, where D is the Drude weight and Γ is the carrier scattering width. **Figure 6**a shows near- and far-infrared extinction spectra (in terms of $1 - T/T_0$, where T and T_0 are the transmissions through graphene and the reference substrate, respectively) of CVD graphene and the different effects that chemical (or electrostatic) doping have on these two regions of the graphene absorption spectra. Analysis of the light extinction in the Drude regime can provide the dynamical conductivity at optical frequencies, the degree of doping (through Pauli blocking), and the carrier mobility (through the scattering rate).[74] In addition to the single-particle interband and intraband excitations of graphene, its collective excitations (i.e., plasmons) are interesting and of technological importance. Graphene can sustain surface plasmons (SPs) propagating along its surface. Because of the different light and plasmon dispersions, the SPs cannot be excited directly by light.[76] However, SP excitation can be achieved by patterning graphene lithographically.[75,77]

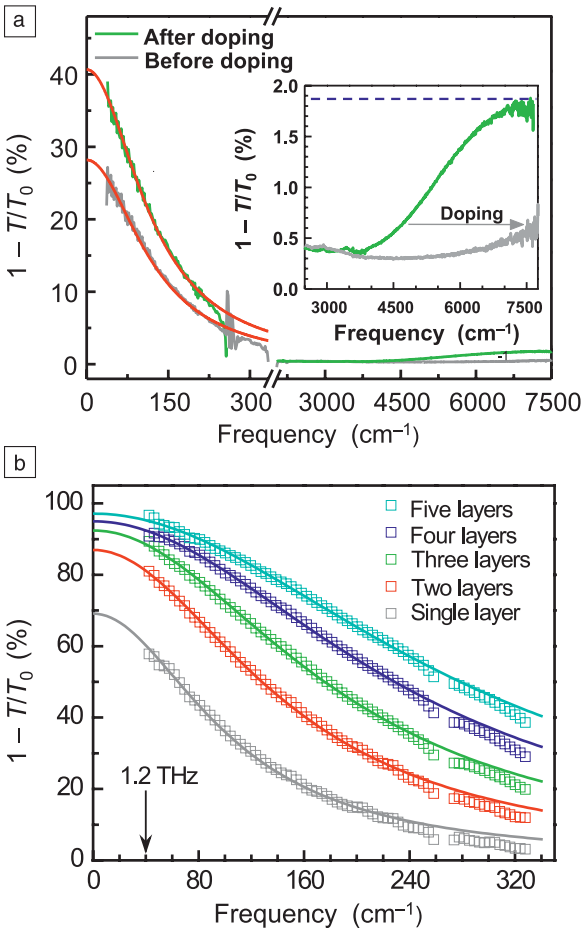

Figure 6. Transmission extinction of graphene, expressed as $1 - T/T_0$, where T and T_0 are the transmissions through graphene on the substrate and through the substrate only, respectively. (Frequency is expressed in wavenumbers [cm^{-1}], with 1 THz ≈ 33.3 cm^{-1}. In terms of equivalent energy, 1 eV ≈ 8000 cm^{-1}.) (a) Near-infrared (right side) and far-infrared (left side) absorption spectra of CVD graphene as transferred onto quartz (gray) and after chemical doping with $(C_2H_5)_3OSbCl_6$ (green). The fit of the data to the Drude model is shown in red. Inset: Expansion showing the effect of doping (Pauli blocking) on the near-infrared spectrum. The blue line shows the 1.9% universal absorption, as corrected for the refractive-index mismatch with quartz. Part (a) reproduced with permission from Reference 74. ©2011, American Chemical Society. (b) Transmission extinction in the terahertz range of CVD graphene superlattices with one, two, three, four, and five layers of graphene. The extinction scales with the number of layers at the higher frequencies, but not at low frequencies. Solid lines are fits to Drude conductivity. Part (b) reproduced with permission from Reference 75. ©2012, Nature Publishing Group.

Research into plasmonics based on noble-metal nanoparticles is highly active and advancing rapidly (as discussed in detail in the August 2012 issue of *MRS Bulletin*),[78] yet graphene offers new opportunities and advantages in plasmonics. These are associated with the extreme confinement, longer SP lifetimes,[76] and longer propagation distances in graphene and, most importantly, with the unique ability to tune the carrier density in graphene electrostatically or chemically.

In patterned graphene structures, strong light–graphene coupling can be used to enhance and tune the optical properties. Both two-dimensional graphene disk arrays and multilayer graphene stacks (superlattices) have been demonstrated that, although transparent in the visible range, can screen out terahertz radiation by means of the plasmons of the ensemble of these layers.[75] These devices were formed by depositing alternating wafer-scale sheets of graphene and thin layers of insulating polymer and then patterning them all together into photonic-crystal-like structures of arrays of columns of circular dots (see **Figure 7**a).[75] It was shown that, as a result of the carrier-concentration scaling law of the plasmonic resonances of Dirac fermions, distributing the carriers into multiple layers strongly enhances the plasmonic resonance frequency and dynamical conductivity at resonance to that obtained by doping single-layer graphene. These structures allowed the construction of widely tunable far-infrared notch filters (see Figure 7b), terahertz linear polarizers, and phase shifters. An unpatterned five-layer graphene stack can shield up to 97.5% of the incident electromagnetic radiation below 1.2 THz (see Figure 6b).

Recent work explored the behavior of these patterned graphene plasmons in a high magnetic field.[79] It was shown that the initial plasmon resonance splits into two, with an energy splitting proportional to the strength of the magnetic field. This effect provides an additional tuning mechanism for the plasmonic absorption of graphene. What is particularly intriguing is that the field tunes not only the energy but also the lifetime of the split plasmons, increasing the lifetime of the lowest-energy branch (edge plasmon) and decreasing the lifetime of the high-energy branch (bulk plasmon).[79]

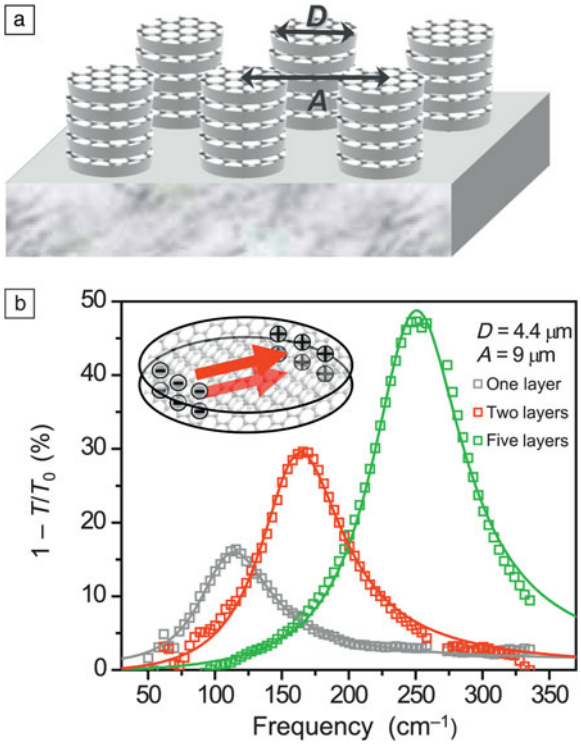

Figure 7. (a) Schematic illustration of the structure of plasmonic graphene/insulator disk stacks arranged in a triangular lattice, showing the disk diameter, *D*, and the array lattice constant, *A*. The graphene plasmonic stacks were formed by patterning the graphene layers into microdisks. (b) Extinction in transmission of plasmonic stacks with one, two, and five graphene layers. Inset: A schematic illustration of dipole coupling in two closely spaced graphene disks, which enhances both the magnitude and frequency of the plasmon resonance. Reproduced with permission from Reference 75. ©2012, Nature Publishing Group.

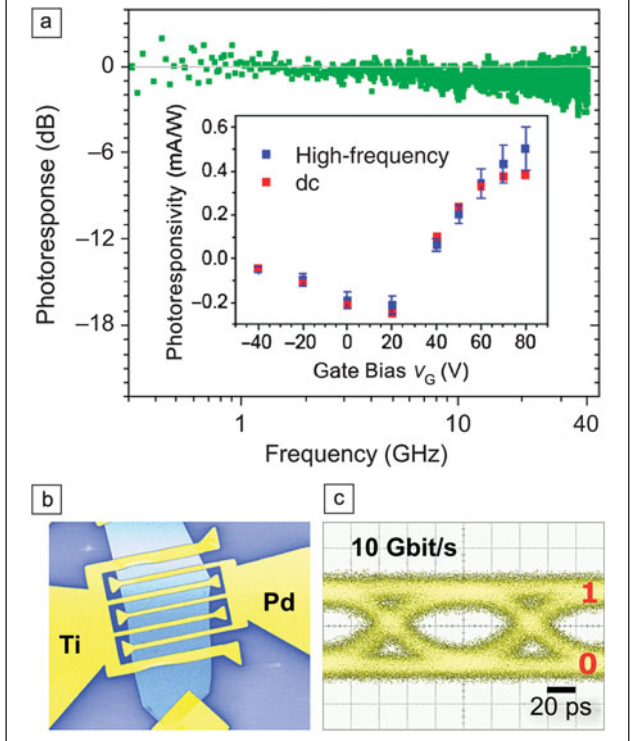

Figure 8. (a) Relative ac photoresponse of a single-contact graphene photodetector as a function of the light-intensity modulation frequency. No degradation of response is seen up to 40 GHz, except for a small degradation of about 1 dB caused by the microwave probes. Inset: Peak dc and high-frequency (ac) photoresponsivities as functions of gate bias. Part (a) reproduced with permission from Reference 80. ©2009, Nature Publishing Group. (b) Interdigitated electrode photodetector based on two different metals: one with a high work function (palladium) and one with a low work function (titanium). This configuration allows enhanced photocurrent generation with full device illumination. (c) Standard receiver "eye diagram" obtained using the interdigitated graphene photodetector to test the detection of optical data streams. The completely "open eye" at a transmission rate of 10 Gbit/s indicates that, at this data rate, there is a time window in which the levels of a digital 1 and 0 can be reliably distinguished. Parts (b) and (c) reproduced with permission from Reference 81. ©2010, Nature Publishing Group.

In terms of active optoelectronic devices employing graphene, the first demonstration of a graphene photodetector was based on a metal–graphene contact. In that case, a metal–graphene junction was irradiated by light in the infrared and visible spectrum.[80] **Figure 8**a shows the measured ac photoresponse of a simple junction detector to a 1.55-μm intensity-modulated light beam. A nearly constant response was observed up to 40 GHz, which was the upper frequency limit of the measurement system. Modeling, however, suggests that, eventually, the detector response will be limited to about 0.6 THz by the *RC* time constant required to charge the device capacitance *C* through its series resistance *R*.[80]

In a symmetric device, simultaneous illumination of both contact regions would produce equal but opposite polarity currents and, therefore, no net photocurrent. The improved design shown in Figure 8b provides a significantly increased photoresponse and allows the full surface of the device to be used for photodetection.[81] This device utilizes interdigitated metal electrodes made of two different metals, one with a high work function and the other with a low work function. These two different work functions produce different doping and band bending in graphene that allows photodetection over the entire area of the device. Photodetectors of this design were shown to reliably detect optical data streams of 1.55-μm light pulses at a rate of 10 Gbit/s[81] (Figure 8c).

Because of the high electron–hole recombination rate in graphene, the photoresponse of graphene detectors is generally modest. To further increase the photoresponse, a number of different approaches have been employed. In one case, enhanced light absorption and photocurrent generation were achieved through excitation of the plasmons of gold nanoparticles deposited on graphene.[82] Another approach involves incorporating graphene inside planar Fabry–Perot microcavities. In one such study, two semitransparent metallic mirrors defined

the resonant cavity, and the graphene was placed at the position of the maximum field, leading to a 20-fold enhancement of the photocurrent at the resonant wavelength.[83] Another study utilized multilayer Bragg reflectors to enhance the reflectance and reported 60% absorption at a resonance wavelength of 850 nm.[84] Most recently, yet another enhancement approach involving the deposition of semiconductor (PbS) quantum dots on graphene was reported.[85]

The ability to modulate the Fermi level of graphene by a gate field naturally leads to its application as a fast electroabsorption modulator.[86] High-speed, small-footprint, and high-bandwidth modulators are highly desirable for optical communications. However, although the interaction of light with graphene is strong considering how thin graphene is, the absorption of a perpendicular light beam by a single graphene layer is insufficient. For this purpose, graphene was integrated with a silicon waveguide to increase the absorption of light traveling parallel to the graphene sheet, and modulation of the guided light by 0.1 dB/μm (from 1.35 μm to 1.6 μm) at frequencies over 1 GHz was demonstrated.[86] An alternative modulator design involving bilayer graphene has also been successfully demonstrated.[87]

Saturable absorption describes the condition whereby the absorption of light by a material decreases with increasing light intensity. Most materials show some saturable absorption, but often only at very high optical intensities (close to the optical damage threshold). Saturable absorbers are used in laser cavities for mode locking and Q switching. With its wide absorption range, fast decay, and high stability, graphene is well-suited for this application and indeed has been successfully used to produce picosecond laser pulses.[88,89]

Conclusions

In summary, graphene is a unique two-dimensional material that offers a wide range of opportunities for applications in electronics and photonics. Key factors are its excellent transport properties and its strong optical response over a very wide wavelength range, especially in the far-infrared and terahertz ranges. Graphene also has the properties of ultimate thinness, flexibility, and mechanical strength in its favor. High-frequency electronic devices and circuits have been successfully demonstrated, as have optoelectronic devices such as fast photodetectors; modulators; and passive optical components such as polarizers, notch filters, and mode lockers. Graphene fabrication can be inexpensive, as carbon is an abundant material and its two-dimensional character allows nanofabrication techniques, already developed in planar silicon technology, to be directly applied. However, significant improvements of the material itself are still required, such as structural homogeneity, layer control, and controllable and stable chemical doping. Better metal contacts and compatible insulators are highly desirable, and performance improvements such as the voltage gain of electronic devices are necessary. Although this article describes only a narrow selection of applications of graphene in electronics and photonics, more innovations that take advantage of the unique properties of graphene are expected in the future.

Acknowledgments

The authors are grateful to Bruce Ek and Jim Bucchignano for technical assistance; Yu-ming Lin, Yanqing Wu, Hugen Yan, Christos Dimitrakopoulos, Alberto Valdes Garcia, Marcus Freitag, Thomas Mueller, Vasili Perebeinos, Mathias Steiner, Wen-juan Zhu, and Xuesong Li for helpful discussions; and the Defense Advanced Research Projects Agency (DARPA) for partial financial support through the Carbon Electronics for RF Applications (CERA) program (Contract FA8650-08-C-7838).

References

1. K.I. Bolotin, K.J. Sikes, Z. Jiang, D.M. Klima, G. Fudenberg, J. Hone, P. Kim, H.L. Stormer, *Solid State Commun.* **146**, 351 (2008).
2. X. Du, I. Skachko, A. Barker, E.Y. Andrei, *Nat. Nanotechnol.* **3**, 491 (2008).
3. F. Schwierz, *Nat. Nanotechnol.* **5**, 487 (2010).
4. A. Balandin, *Nat. Nanotechnol.* **10**, 569 (2011).
5. S. Adam, E.H. Hwang, V.M. Galitski, S. Das Sarma, *Proc. Natl. Acad. Sci. U.S.A.* **104**, 18392 (2007).
6. J.-H. Chen, C. Jang, M. Ishigami, S. Xiao, W.G. Gullen, E.D. Williams, M.S. Fuhrer, *Solid State Commun.* **149**, 1080 (2009).
7. J.-H. Chen, C. Chaun, C. Jang, S. Xiao, M. Ishigami, M.S. Fuhrer, *Nat. Nanotechnol.* **3**, 206 (2008).
8. K. Nomura, A.H. MacDonald, *Phys. Rev. Lett.* **96**, 256602 (2006).
9. W. Zhu, V. Perebeinos, M. Freitag, Ph. Avouris, *Phys. Rev. B* **80**, 235402 (2009).
10. M.I. Katsnelson, A.K. Geim, *Philos. Trans. R. Soc. A* **366**, 195 (2008).
11. D.B. Farmer, V. Perebeinos, Y.-M. Lin, C. Dimitrakopoulos, Ph. Avouris, *Phys. Rev. B* **84**, 205417 (2011).
12. J.-H. Chen, W.G. Cullen, C. Jang, M.S. Fuhrer, E.D. Williams, *Phys. Rev. Lett.* **102**, 236805 (2009).
13. T. Ando, *J. Phys. Soc. Jpn.* **75**, 074716 (2006).
14. J.-H. Chen, C. Jang, M. Ishigami, S. Xiao, W.G. Cullen, E.D. Williams, M.S. Fuhrer, *Solid State Commun.* **149**, 1080 (2009).
15. Y. Wu, V. Perebeinos, Y.-M. Lin, T. Low, F. Xia, Ph. Avouris, *Nano Lett.* **12**, 1417 (2012).
16. Y.-W. Tan, Y. Zhang, K. Bolotin, Y. Zhao, S. Adam, E.H. Hwang, S. Das Sarma, H.L. Stormer, P. Kim, *Phys. Rev. Lett.* **99**, 246803 (2007).
17. Y. Wu, K.A. Jerkins, A. Valdes-Garcia, D.B. Farmer, Y. Zhu, A.A. Bol, C. Dimitrakopoulos, W. Zhu, F. Xia, Ph. Avouris, Y.-M. Lin, *Nano Lett.* **12**, 3062 (2012).
18. G. Giovannetti, P.A. Khomyakov, G. Brocks, V.M. Karpan, J. van den Brink, P.J. Kelly, *Phys. Rev. Lett.* **101**, 026803 (2008).
19. P.A. Khomyakov, G. Giovannetti, P.C. Rusu, G. Brocks, J. van den Brink, P.J. Kelly, *Phys. Rev. B* **79**, 195425 (2009).
20. F. Xia, V. Perebeinos, Y.-M. Lin, Y. Wu, Ph. Avouris, *Nat. Nanotechnol.* **6**, 179 (2011).
21. B. Huard, N. Stander, J.A. Sulpizio, D. Goldhaber-Gordon, *Phys. Rev. B* **78**, 121402 (2008).
22. J. Cayssol, B. Huard, D. Goldhaber-Gordon, *Phys. Rev. B* **79**, 075428 (2009).
23. K.S. Novoselov, A.K. Geim, S.V. Morozov, D. Jiang, Y. Zhang, S.V. Dubonos, I. Grigorieva, A.A. Firsov, *Science* **306**, 666 (2004).
24. D.V. Badami, *Nature* **193**, 569 (1962).
25. A.J. van Bommel, J.E. Crombeen, A. van Tooren, *Surf. Sci.* **48**, 463 (1975).
26. I. Forbeaux, J.-M. Themlin, A. Charrier, F. Thibaudau, J.-M. Debever, *Appl. Surf. Sci.* **162–163**, 406 (2000).
27. C. Berger, Z. Song, T. Li, X. Li, A.Y. Ogbazghi, R. Feng, Z. Dai, A.N. Marchenkov, E.H. Conrad, P.N. First, W.A. de Heer, *J. Phys. Chem. B* **108**, 19912 (2004).
28. Ph. Avouris, C. Dimitrakopoulos, *Mater. Today* **15**, 86 (2012).
29. J.W. May, *Surf. Sci.* **17**, 267 (1969).
30. A. Reina, X. Jia, J. Ho, D. Nezich, H. Son, V. Bulovic, M.S. Dresselhaus, J. Kong, *Nano Lett.* **9**, 30 (2009).
31. X. Li, W. Cai, J. An, S. Kim, J. Nah, D. Yang, R.D. Piner, A. Velamakanni, I. Jung, E. Tutuc, S.K. Banerjee, L. Colombo, R.S. Ruoff, *Science* **324**, 1312 (2009).

32. S. Chen, W. Cai, R.D. Piner, J.W. Suk, Y. Wu, Y. Ren, J. Kang, R.S. Ruoff, *Nano Lett.* **11**, 3519 (2011).
33. D.B. Farmer, H.-Y. Chiu, Y.-M. Lin, K. Jenkins, F. Xia, Ph. Avouris, *Nano Lett.* **9**, 4474 (2009).
34. W. Zhu, D. Neumayer, V. Perebeinos, Ph. Avouris, *Nano Lett.* **10**, 3572 (2010).
35. S. Kim, J. Nah, I. Jo, D. Shahrjerdi, L. Colombo, Z. Yao, E. Tutuc, S.K. Banerjee, *Appl. Phys. Lett.* **94**, 062107 (2009).
36. Y. Wu, D.B. Farmer, A. Valdes-Garcia, W. Zhu, K.A. Jenkins, C. Dimitrakopoulos, Ph. Avouris, Y.-M. Lin, *Tech. Dig.–Int. Electron Devices Meet.* 6131601 (2011).
37. Y. Wu, Y.-M. Lin, A.A. Bol, K.A. Jenkins, F. Xia, D.B. Farmer, Y. Zhu, Ph. Avouris, *Nature* **472**, 74 (2011).
38. M.C. Lemme, T.J. Echtermeyer, M. Baus, J. Kurz, *IEEE Electron Device Lett.* **28**, 282 (2007).
39. J. Kedzierski, P.L. Hsu, P. Healey, P.W. Wyatt, C.L. Keast, M. Sprinkle, C. Berger, W.A. de Heer, *IEEE Trans. Electron Devices* **55**, 2078 (2008).
40. I. Meric, N. Baklitskaya, P. Kim, K.L. Shepard, *Tech. Dig.–Int. Electron Devices Meet.* 4796738 (2008).
41. J.S. Moon, D. Curtis, M. Hu, D. Wong, C. McGuire, P.M. Campbell, G. Jernigan, J.L. Tedesco, B. VanMil, R. Myers-Ward, C. Eddy, D.K. Gaskill, *IEEE Electron Device Lett.* **30**, 650 (2009).
42. Y.-M. Lin, K.A. Jenkins, A. Valdes-Garcia, J.P. Small, D.B. Farmer, Ph. Avouris, *Nano Lett.* **9**, 422 (2009).
43. Y.-M. Lin, C.-Y. Chiu, K.A. Jenkins, D.B. Farmer, Ph. Avouris, *IEEE Electron Device Lett.* **31**, 68 (2010).
44. Y.-M. Lin, C. Dimitrakopoulos, K.A. Jenkins, D.B. Farmer, H.-Y. Chiu, A. Grill, Ph. Avouris, *Science* **327**, 662 (2010).
45. L. Liao, Y. Lin, M. Bao, R. Cheng, J. Bai, Y. Liu, Y. Qu, K.L. Wang, Y. Huang, X. Duan, *Nature* **467**, 305 (2010).
46. Y.-M. Lin, A. Valdes-Garcia, S.-J. Han, D.B. Farmer, I. Meric, Y. Sun, Y. Wu, C. Dimitrakopoulos, A. Grill, Ph. Avouris, K.A. Jenkins, *Science* **332**, 1294 (2011).
47. C.R. Dean, A.F. Young, I. Meric, C. Lee, L. Wang, S. Sorgenfrei, K. Watanabe, T. Taniguchi, P. Kim, K.L. Shepard, J. Hone, *Nat. Nanotechnol.* **5**, 722 (2010).
48. L. Britnell, R.V. Gorbachev, R. Jalil, B.D. Belle, F. Schedin, A. Mishchenko, T. Georgiou, M.I. Katsnelson, L. Eaves, S.V. Morozov, N.M. R. Peres, J. Leist, A.K. Geim, K.S. Novoselov, L.A. Ponomarenko, *Science* **335**, 947 (2012).
49. J. Xue, J. Sanchez-Yamagishi, D. Bulmash, P. Jacquod, A. Deshpande, K. Watanabe, T. Taniguchi, P. Jarillo-Herrero, B.J. LeRoy, *Nat. Mater.* **10**, 282 (2011).
50. R. Decker, Y. Wang, V.W. Brar, W. Regan, H. Tsai, Q. Wu, W. Gannett, A. Zettl, M.F. Crommie, *Nano Lett.* **11**, 2291 (2011).
51. Z. Liu, L. Song, S. Zhao, J. Huang, L. Ma, J. Zhang, J. Lou, P.M. Ajayan, *Nano Lett.* **11**, 2032 (2011).
52. W. Han, A. Hsu, J. Wu, J. Kong, T. Palacios, *IEEE Electron Device Lett.* **31**, 906 (2010).
53. E. Guerriero, L. Polloni, L. Giorgi Rizzi, M. Bianchi, G. Mondello, R. Sordan, *Small* 357 (2012).
54. S.-J. Han, K.A. Jenkins, A. Valdes-Garcia, A.D. Franklin, A.A. Bol, W. Haensch, *Nano Lett.* **11**, 3690 (2011).
55. R.R. Nair, P. Blake, A.N. Grigorenko, K.S. Novoselov, T.J. Booth, T. Stauber, N.M.R. Peres, A.K. Geim, *Science* **320**, 1308 (2008).
56. A.B. Kuzmenko, E. Van Heumen, F. Carbone, D. van der Marel, *Phys. Rev. Lett.* **100**, 117401 (2008).
57. K.F. Mak, M.Y. Sfeir, Y. Wu, C. Lui, J.A. Misewich, T.F. Heinz, *Phys. Rev. Lett.* **101**, 196405 (2008).
58. F. Wang, Y. Zhang, C. Tian, C. Girit, A. Zettl, M. Crommie, Y.R. Shen, *Science* **320**, 206 (2008).
59. K.F. Mak, J. Shan, T.F. Heinz, *Phys. Rev. Lett.* **106**, 046401 (2011).
60. D.H. Chae, T. Utikal, S. Weisenburger, H. Giessen, K.v. Klitzing, M. Lippitz, J. Smet, *Nano Lett.* **11**, 1379 (2011).
61. L. Yang, M.L. Cohen, S.G. Louie, *Nano Lett.* **7**, 3112 (2007).
62. E. Malic, T. Winzer, E. Bobkin, A. Knorr, *Phys. Rev. B* **84**, 205406 (2011).
63. R. Kim, V. Perebeinos, Ph. Avouris, *Phys. Rev. B* **84**, 075449 (2011).
64. R. Bistritzer, A.H. MacDonald, *Phys. Rev. Lett.* **102**, 206410 (2009).
65. D.B. Farmer, R. Golizadeh-Mojarad, V. Perebeinos, Y.-M. Lin, G.S. Tulevski, J.C. Tsang, Ph. Avouris, *Nano Lett.* **9**, 388 (2009).
66. J.R. Williams, L. DiCarlo, C.M. Marcus, *Science* **317**, 638 (2007).
67. E.J.H. Lee, K. Balasubramanian, R.T. Weitz, M. Burghard, K. Kern, *Nat. Nanotechnol.* **3**, 486 (2008).
68. J. Park, Y.H. Ahn, C. Ruiz-Vargas, *Nano Lett.* **9**, 1742 (2009).
69. F. Xia, T. Mueller, R. Golizadeh-Mojarad, M. Freitag, Y.-M. Lin, J.C. Tsang, V. Perebeinos, Ph. Avouris, *Nano Lett.* **9**, 1039 (2009).
70. T. Mueller, F. Xia, M. Freitag, J.C. Tsang, Ph. Avouris, *Phys. Rev. B* **79**, 245430 (2009).
71. X. Xu, N.M. Gabor, J.S. Alden, A.M. van der Zande, P.L. McEuen, *Nano Lett.* **10**, 562 (2010).
72. J.C. Song, M.S. Rudner, C.M. Marcus, L.S. Levitov, *Nano Lett.* **11**, 4688 (2011).
73. N.M. Gabor, J.C.W. Song, Q. Ma, N.L. Nair, T. Taychatanapwat, K. Watanabe, T. Taniguchi, L.S. Levitov, P. Jarillo-Herrero, *Science* **334**, 648 (2011).
74. H. Yan, F. Xia, W. Zhu, M. Freitag, C. Dimitrakopoulos, A.A. Bol, G. Tulevski, Ph. Avouris, *ACS Nano* **5**, 9854 (2011).
75. H. Yan, X. Li, B. Chandra, G. Tulevski, Y. Wu, M. Freitag, W. Zhu, Ph. Avouris, F. Xia, *Nat. Nanotechnol.* **7**, 330 (2012).
76. F.H.L. Koppens, D.E. Chang, F.J. García de Abajo, *Nano Lett.* **11**, 3370 (2011).
77. L. Ju, B. Geng, J. Horng, C. Girit, M. Martin, Z. Hao, H.A. Bechtel, X. Liang, A. Zettl, Y.R. Shen, F. Wang, *Nat. Nanotechnol.* **6**, 630 (2011).
78. N. Halas, N.S. Lal, W.-S. Chang, S. Link, P. Nordlander, *Chem. Rev.* **111**, 3913 (2011).
79. H. Yan, Z. Li, X. Li, W. Zhu, Ph. Avouris, F. Xia, *Nano Lett.* **12**, 3766 (2012).
80. F. Xia, T. Mueller, Y.-M. Lin, A. Valdes-Garcia, Ph. Avouris, *Nat. Nanotechnol.* **4**, 839 (2009).
81. T. Mueller, F. Xia, Ph. Avouris, *Nat. Photonics* **4**, 297 (2010).
82. T.J. Echtermeyer, L. Britnell, P.K. Jasnos, A. Lombardo, R.V. Gorbachev, A.N. Grigorenko, A.K. Geim, A.C. Ferrari, K.S. Novoselov, *Nat. Commun.* **2**, 458 (2011).
83. M. Engel, M. Steiner, A. Lombardo, A.C. Ferrari, H.v. Loehneysen, Ph. Avouris, R. Krupke, *Nat. Commun.* **3**, 906 (2011).
84. M. Furchi, A. Urich, A. Pospischil, G. Lilley, K. Unterrainer, H. Detz, P. Klang, A.M. Andrews, W. Schrenk, G. Strasser, T. Mueller, *Nano Lett.* **12**, 2773 (2012).
85. G. Konstantatos, M. Badioli, L. Gaudreau, J. Osmond, M. Bernechea, P.G. de Arquer, F. Gatti, F.H.L. Koppens, *Nat. Nanotechnol.* **7**, 363 (2012).
86. M. Liu, X. Yin, E. Ulin-Avila, B. Geng, T. Zentgraf, L. Ju, F. Wang, X. Zhang, *Nature* **474**, 64 (2011).
87. M. Liu, X. Yin, X. Zhang, *Nano Lett.* **12**, 1482 (2012).
88. Q.L. Bao, H. Zhang, Y. Wang, Z. Ni, Y. Yan, Z. Shen, K. Loh, D. Tang, *Adv. Funct. Mater.* **19**, 3077 (2009).
89. Z. Sun, T. Hasan, F. Torrisi, D. Popa, G. Privitera, F. Wang, F. Bonaccorso, D.M. Basko, A.C. Ferrari, *ACS Nano* **4**, 803 (2010). □